

Optical generation of single-cycle 10 MW peak power 100 GHz waves

XIAOJUN WU,^{1,2,5} ANNE-LAURE CALENDRON,^{1,2,5,*} KOUSTUBAN RAVI,^{1,3} CHUN ZHOU,^{1,4} MICHAEL HEMMER,¹ FABIAN REICHERT,^{1,4} DONGFANG ZHANG,^{1,4} HUSEYIN CANKAYA,^{1,2} LUIS E. ZAPATA,¹ NICHOLAS H. MATLIS,¹ AND FRANZ X. KÄRTNER^{1,2,3,4}

¹Center for Free-Electron Laser Science, Deutsches Elektronen Synchrotron, Notkestrasse 85, 22607 Hamburg, Germany

²Centre for Ultrafast Imaging, University of Hamburg, Luruper Chaussee 149, 22761 Hamburg, Germany

³Department of Electrical Engineering and Computer Science and Research Laboratory of Electronics, MIT, Cambridge, 02139 Massachusetts, USA

⁴Department of Physics, University of Hamburg, Luruper Chaussee 149, 22761 Hamburg, Germany

⁵These authors contributed equally to this work

*anne-laure.calendron@desy.de

Abstract: We demonstrate the generation of 100 GHz single-cycle pulses with up to 10 MW of peak power using optical rectification and broadband phase matching via the tilted pulse front (TPF) technique in lithium niobate. The optical driver is a cryogenically cooled Yb:YAG amplifier providing tens of mJ energy, ~5 ps long laser pulses. We obtain a high THz pulse energy up to 65 μ J with 31.6 MV/m peak electric field when focused close to its diffraction limit of 2.5 mm diameter. A high optical-to-THz energy conversion efficiency of 0.3% at 85 K is measured in agreement with numerical simulations. This source is of great interest for a broad range of applications, such as nonlinear THz field-matter interaction and charged particle acceleration for ultrafast electron diffraction and table-top X-ray sources.

© 2016 Optical Society of America

OCIS codes: (320.7110) Ultrafast nonlinear optics; (320.7160) Ultrafast technology; (140.3070) Infrared and far-infrared lasers.

References and links

1. T. Maag, A. Bayer, S. Baierl, M. Hohenleutner, T. Korn, C. Schüller, D. Schuh, D. Bougeard, C. Lange, R. Huber, M. Mootz, J. E. Sipe, S. W. Koch, and M. Kira, "Coherent cyclotron motion beyond Kohn's theorem," *Nat. Phys.* **12**(2), 119–123 (2015).
2. R. Matsunaga, N. Tsuji, H. Fujita, A. Sugioka, K. Makise, Y. Uzawa, H. Terai, Z. Wang, H. Aoki, and R. Shimano, "Light-induced collective pseudospin precession resonating with Higgs mode in a superconductor," *Science* **345**(6201), 1145–1149 (2014).
3. M. Sherwin, "Terahertz power," *Nature* **420**(6912), 131–133 (2002).
4. M. Tonouchi, "Cutting-edge terahertz technology," *Nat. Photonics* **1**(2), 97–105 (2007).
5. O. Schubert, M. Hohenleutner, F. Langer, B. Urbanek, C. Lange, U. Huttner, D. Golde, T. Meier, M. Kira, S. W. Koch, and R. Huber, "Sub-cycle control of terahertz high-harmonic generation by dynamical Bloch oscillations," *Nat. Photonics* **8**(2), 119–123 (2014).
6. K. Iwaszczuk, M. Zalkovskij, A. C. Strikwerda, and P. U. Jepsen, "Nitrogen plasma formation through terahertz-induced ultrafast electron field emission," *Optica* **2**(2), 116 (2015).
7. M. R. Siegrist, H. Bindslev, R. Brazis, D. Guyomarc'h, J. P. Hogge, Ph. Moreau, and R. Raguotis, "Development of a high-power THz radiation source for plasma diagnostics," *Infrared Phys. Technol.* **40**(3), 247–259 (1999).
8. K. N. Egodapitiya, S. Li, and R. R. Jones, "Terahertz-induced field-free orientation of rotationally excited molecules," *Phys. Rev. Lett.* **112**(10), 103002 (2014).
9. Y.-C. Shen and P. F. Taday, "Development and application of terahertz pulsed imaging for nondestructive inspection of pharmaceutical tablet," *IEEE J. Sel. Top. Quantum Electron.* **14**(2), 407–415 (2008).
10. E. A. Nanni, W. R. Huang, K.-H. Hong, K. Ravi, A. Fallahi, G. Moriena, R. J. D. Miller, and F. X. Kärtner, "Terahertz-driven linear electron acceleration," *Nat. Commun.* **6**, 8486 (2015).
11. W. R. Huang, E. A. Nanni, K. Ravi, K.-H. Hong, A. Fallahi, L. J. Wong, P. D. Keathley, L. E. Zapata, and F. X. Kärtner, "Toward a terahertz-driven electron gun," *Sci. Rep.* **5**, 14899 (2015).

12. C. Kealhofer, W. Schneider, D. Ehberger, A. Ryabov, F. Krausz, and P. Baum, "All-optical control and metrology of electron pulses," *Science* **352**(6284), 429–433 (2016).
13. A. Zholents, "A new possibility for production of sub-picosecond X-ray pulses using a time dependent radio frequency orbit deflection," *Nucl. Instr. Meth. Phys. Res.* **798**, 111–116 (2015).
14. F. X. Kärtner, F. Ahr, A.-L. Calendron, H. Cankaya, S. Carbajo, G. Chang, G. Cirmi, K. Dörner, U. Dorda, A. Fallahi, T. Hartin, M. Hemmer, R. Hobbs, Y. Hua, R. Huang, R. Letrun, N. Matlis, V. Mazalova, O. Mücke, E. Nanni, W. Putnam, K. Ravi, F. Reichert, I. Sarrou, X. Wu, H. Ye, L. Zapata, D. Zhang, C. Zhou, R. J. D. Miller, K. Berggren, H. Graafsma, A. Meents, R. W. Assmann, H. N. Chapman, and P. M.-L. Fromme, "AXSIS: Exploring the Frontiers in Attosecond X-ray Science, Imaging and Spectroscopy," *NIMA Proceedings* (2016).
15. A. Fallahi, M. Fakhari, A. Yahaghi, M. Arrieta, and F. X. Kärtner, "Short Electron Bunch Generation Using Single-cycle Ultrafast Electron Guns," arXiv:1606.02153 (2016).
16. S. H. Gold and G. S. Nusinovich, "Review of high-power microwave source research," *Rev. Sci. Instrum.* **68**(11), 3945 (1997).
17. N. Yardimici, S.-H. Yang, C. W. Berr, and M. Jarrahi, "High-power terahertz generation using large-area plasmonic photoconductive emitters," *IEEE Trans. THz Sci. and Tech.* **5**(2), 223–229 (2015).
18. B. Lax, R. L. Aggarwal, and G. Favrot, "Far-infrared step-tunable coherent radiation source: 70 μm to 2 mm," *Appl. Phys. Lett.* **23**(12), 679 (1973).
19. C. Vicario, A. V. Ovchinnikov, S. I. Ashitkov, M. B. Agranat, V. E. Fortov, and C. P. Hauri, "Generation of 0.9-mJ THz pulses in DSTMS pumped by a Cr:Mg₂SiO₄ laser," *Opt. Lett.* **39**(23), 6632–6635 (2014).
20. M. A. Piestrup, R. N. Fleming, and R. H. Pantell, "Continuously tunable submillimeter wave source," *Appl. Phys. Lett.* **26**(8), 418 (1975).
21. K. Kawase, M. Sato, T. Tanuichi, and H. Ito, "Coherent tunable THz-wave generation from LiNbO₃ with monolithic grating coupler," *Appl. Phys. Lett.* **68**(18), 2483 (1996).
22. J. Hebling, G. Almási, I. Kozma, and J. Kuhl, "Velocity matching by pulse front tilting for large area THz-pulse generation," *Opt. Express* **10**(21), 1161–1166 (2002).
23. J. A. Fülöp, Z. Ollmann, C. Lombosi, C. Skrobol, S. Klingebiel, L. Pálfalvi, F. Krausz, S. Karsch, and J. Hebling, "Efficient generation of THz pulses with 0.4 mJ energy," *Opt. Express* **22**(17), 20155–20163 (2014).
24. S.-W. Huang, E. Granados, W. R. Huang, K.-H. Hong, L. E. Zapata, and F. X. Kärtner, "High conversion efficiency, high energy terahertz pulses by optical rectification in cryogenically cooled lithium niobate," *Opt. Lett.* **38**(5), 796–798 (2013).
25. W. R. Huang, S. W. Huang, E. Granados, K. Ravi, K. H. Hong, L. E. Zapata, and F. X. Kärtner, "Highly efficient terahertz pulse generation by optical rectification in stoichiometric and cryo-cooled congruent lithium niobate," *J. Mod. Opt.* **62**(18), 1486–1493 (2015).
26. L. E. Zapata, F. Reichert, M. Hemmer, and F. X. Kärtner, "250 W average power, 100 kHz repetition rate cryogenic Yb:YAG amplifier for OPCPA pumping," *Opt. Lett.* **41**(3), 492–495 (2016).
27. C. M. Baumgarten, B. A. Reagan, M. A. Pedicone, H. Bravo, L. Yin, H. Wang, M. Woolston, B. Carr, C. S. Menoni, and J. J. Rocca, "Demonstration of a Compact 500 Hz Repetition Rate Joule-Level Chirped Pulse Amplification Laser," *CLEO Digest*, paper STu3M.3 (2016).
28. J. Hebling, K.-L. Yeh, M. C. Hoffmann, B. Bartal, and K. A. Nelson, "Generation of high-power terahertz pulses by tilted-pulse-front excitation and their application possibilities," *J. Opt. Soc. Am. B* **25**(7), B6 (2008).
29. M. Unferdorben, Z. Szaller, I. Hajdara, J. Hebling, and L. Pálfalvi, "Measurement of refractive index and absorption coefficient of congruent and stoichiometric lithium niobate in the terahertz range," *J. Infrared Milli Terahz Waves* **36**(12), 1203–1209 (2015).
30. X. Wu, C. Zhou, W. R. Huang, F. Ahr, and F. X. Kärtner, "Temperature dependent refractive index and absorption coefficient of congruent lithium niobate crystals in the terahertz range," *Opt. Express* **23**(23), 29729–29737 (2015).
31. K. Ravi, W. R. Huang, S. Carbajo, X. Wu, and F. Kärtner, "Limitations to THz generation by optical rectification using tilted pulse fronts," *Opt. Express* **22**(17), 20239–20251 (2014).
32. F. Blanchard, X. Ropagnol, H. Hafez, H. Razavipour, M. Bolduc, R. Morandotti, T. Ozaki, and D. G. Cooke, "Effect of extreme pump pulse reshaping on intense terahertz emission in lithium niobate at multimillijoule pump energies," *Opt. Lett.* **39**(15), 4333–4336 (2014).
33. K. H. Yang, P. L. Richards, and Y. R. Shen, "Generation of far-infrared radiation by picosecond light pulses in LiNbO₃," *Appl. Phys. Lett.* **19**(9), 320–323 (1971).
34. K. Ravi, W. R. Huang, S. Carbajo, E. A. Nanni, D. N. Schimpf, E. P. Ippen, and F. X. Kärtner, "Theory of terahertz generation by optical rectification using tilted-pulse-fronts," *Opt. Express* **23**(4), 5253–5276 (2015).
35. A.-L. Calendron, H. Cankaya, and F. X. Kärtner, "High-energy kHz Yb:KYW dual-crystal regenerative amplifier," *Opt. Express* **22**(20), 24752–24762 (2014).
36. R. S. Weis and T. K. Gaylord, "Lithium niobate: summary of physical properties and crystal structure," *Appl. Phys., A Mater. Sci. Process.* **37**(4), 191–203 (1985).
37. G. Dmitriev, G. G. Gurzadyan, and D. N. Nikogosyan, *Handbook of Nonlinear Crystals* (Berlin Spring Verlag, (1999).
38. T. Kampfrath, K. Tanaka, and K. A. Nelson, "Resonant and nonresonant control over matter and light by intense terahertz transients," *Nat. Photonics* **7**(9), 680–690 (2013).
39. C. Lombosi, G. Polónyi, M. Mechler, Z. Ollmann, J. Hebling, and J. A. Fülöp, "Nonlinear distortion of intense THz beams," *New J. Phys.* **17**(8), 083041 (2015).

1. Introduction

The terahertz (THz) frequency range between 0.1 and 1 THz (or wavelength range of 0.3-3 mm) offers great opportunities in science [1–5]. The lack of bright, single or few-cycle, cost effective, THz sources with simultaneously high peak fields and large pulse energies has however been the bottleneck for research topics such as high order harmonic generation in solids [5], investigation of plasma formation [6], exploration of plasma diagnostics [7], and molecular spectroscopy [8]. Such source technology could also support industrial applications, like non-destructive inspection [9], and global environmental sensing [4]. The low frequency range is also interesting for electron acceleration [10], ultrafast electron diffraction and compact x-ray sources. In the acceleration process, the maximum bunch charge that can be accelerated is proportional to the wavelength of the accelerating field [10–12]. Moreover, using frequencies lower than 0.3 THz, *i.e.* a wavelength longer than 1 mm increases the size of the acceleration devices and thus alleviates fabrication challenges. Lower frequency THz radiation may also be useful for electron beam diagnostics using deflecting cavities [13]. However, for electron acceleration (possibly up to relativistic speeds) or diagnostic applications, single-cycle THz pulses with pulse energies of several-mJ (~ 10 mJ) [14,15] at high repetition rates (>100 Hz) are required.

Among various approaches, THz waves can be generated either in large facilities such as free-electron lasers, which are limited in their user accessibility, or via gyrotrons which while relatively efficient are limited to long THz pulse durations (≥ 1 μ s) [16], or by photoconductive switches [17], which are challenging to scale to large pulse energies. On the opposite, nonlinear conversion [18] of high-energy optical pulses obtained from table-top laser systems are amenable for the generation of single-cycle THz pulses with high pulse energies. The latter technique overcomes the limitations of the first ones in terms of output THz peak power and therefore electric field strength, at the expense of the wall-plug to THz radiation conversion efficiency decreasing from 25 to 50% for the gyrotrons to $1\text{--}10 \times 10^{-5}$ for optical lasers.

The optical-to-THz energy conversion efficiency obtained from nonlinear conversion processes depends on the method chosen for generating THz radiation. Single-cycle THz generation by optical rectification in organic materials has yielded conversion efficiencies as high as 3% but is limited to frequencies > 1 THz, due to THz absorption [19]. It also requires pumping at wavelengths > 1.3 μ m, where construction of high energy, high repetition rate laser systems is challenging. Another prospective approach, THz generation in lithium niobate [20,21], was extended to large THz bandwidths by optical rectification of tilted-pulse-fronts [22]. This approach can reach conversion efficiencies up to the percent level [23–25], overcoming the Manley-Rowe limit by repeated energy down conversion of the pump photons in a process known as cascading. The generation of THz pulses with tens of mJ energy with this approach can thus be enabled by Joule-class ~ 1 μ m laser systems, which are realized at high repetition rates using cryogenically cooled Yb:YAG amplifiers [26,27]. This laser technology is promising for high energy, high power laser amplifiers due to the improved thermo-optical properties and high gain at cryogenic temperature; the spectral width sustained is however < 0.5 nm resulting in ps-level pulse duration. This spectral bandwidth is however well suited to the generation of the aforementioned low frequency THz radiation at 0.1 THz.

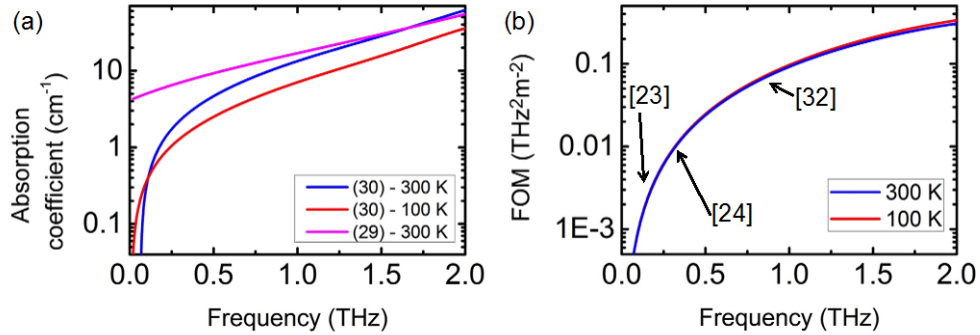


Fig. 1. (a) Absorption coefficient of 6% MgO doped lithium niobate at room temperature [20,21] and cryogenic temperature [21] along the crystallographic z-axis. The data from [20,21] has been extrapolated from 250 GHz and 400 GHz, respectively, below 100 GHz. (b) Figure of merit taking into account the THz frequency Ω^2 and the absorption coefficient α . Previous works are indicated.

Equation (1), taken from [28], expresses the conversion efficiency η_{THz} for conversion of driving pulse energy into THz radiation in the undepleted pump approximation: it depends on the material parameters (effective nonlinear coefficient d_{eff} , absorption coefficient α , refractive index at driver wavelength n_{opt} and THz wavelength n_{THz}), length L and driver intensity I and scales with the square of the THz frequency Ω :

$$\eta_{THz} = \frac{2d_{eff}^2}{\epsilon_0 n_{opt}^2 n_{THz} c^3} \Omega^2 I L^2 e^{-\alpha L/2} \frac{\sinh^2(\alpha L/4)}{(\alpha L/4)^2} \quad (1)$$

Therefore, if absorption is neglected, a reduction in THz frequency from 0.3 THz down to 0.1 THz would decrease the conversion efficiency by nearly an order of magnitude. However, the variation of absorption with THz frequency in the material mitigates this effect: the absorption coefficient decreases from 10.1 cm⁻¹ for 0.5 THz frequency to 4.1 cm⁻¹ at 0.25 THz in lithium niobate, on the extraordinary axis, at room temperature [28]; this decreasing behavior can be further extrapolated via a Voigt function to 0 THz frequency. The absorption coefficient along the extraordinary axis of congruent lithium niobate (cLN) is given in Fig. 1(a) for different temperatures, from the measurements of [29,30]. Decreasing the temperature leads to a reduced absorption of the generated THz radiation; as the conversion efficiency depends on the crystal length quadratically, it consequently increases in a parabolic manner with lower THz absorption. These effects are displayed as in Fig. 1(b) by a figure of merit (FOM) for THz generation defined from Eq. (1), taking into account the terms depending on the THz frequency and crystal length, setting the crystal length to 1 cm, and scaled between 0 and 1: a change in the THz frequency of 0.3 THz to 0.1 THz at room temperature induces a decrease of the FOM from 0.005 THz²/m² to 0.001 THz²/m². This disparity between the FOMs at the two frequencies is expected to further reduce upon consideration of cascading effects, which in conjunction with angular dispersion were shown to dramatically limit the conversion efficiencies obtained by the use of tilted-pulse-fronts [31,32]. The key point being that the disparity in conversion efficiencies between large and small THz frequencies may not be sufficiently large to outrun the advantage of highly accessible pump laser energy at small bandwidths. This makes low THz frequency generation a competitive prospect for generating very high THz pulse energies on the order of 10 mJ, suited to the aforementioned applications. In Fig. 1(b), some references to previous works generating THz radiation at higher frequencies are given.

Recently, high energy, strong-field single-cycle THz pulses with high optical-to-THz energy conversion efficiencies at the percent level and half-percent level from 1030 nm

[24,25] and 800 nm [32] wavelengths have been respectively generated at frequencies between 0.3 THz and 0.4 THz, using broadband phase matching via the tilted pulse front (TPF) method in lithium niobate crystals [22]. By optimizing the pulse duration, up to 0.77% conversion efficiency were demonstrated at 0.2 THz frequency [23]. Earlier, THz radiation was reported between 3 and 22 cm^{-1} , corresponding to 90 to 660 THz frequencies, with low efficiency and peak power of 200W [33]. Here, for the first time to our knowledge, we apply the TPF method to high-energy, narrow-band, ps long laser pulses to generate intense 0.1 THz pulses.

In this work, we use tens of mJ, 4.7-ps, 100-Hz, 1030-nm Yb:YAG laser pulses to generate THz pulses via optical rectification in lithium niobate. We obtained single-cycle THz pulses with a record peak field of 31.6 MV/m at the THz frequency of 0.1 THz when tightly focused. The achieved THz output energy is 65 μJ with an energy conversion efficiency of 0.3% in agreement with theoretical predictions. Spatio-temporal (2 + 1-D) simulations accounting for all spatio-temporal distortions imparted to the infrared (IR) pulse by the TPF setup, cascading effects, Kerr and Raman effects were performed to prepare and confirm the experiments [34]. The spatio-temporal distortions include temporal and spatial chirp as well as angular dispersion. The experimental results are in agreement with the simulation results.

2. Experimental setup

The experimental setup includes two parts: a high energy pump laser and a tilted pulse front (TPF) setup shown in Fig. 2(a). A fraction of the 5.5 mJ output of a dual-crystal Yb:KYW regenerative amplifier [35] is used to seed a cryogenically cooled Yb:YAG rod-type multi-pass amplifier operating at 100 Hz repetition rate. The rod amplifier narrows the 3.5 nm wide input spectrum down to 0.31 nm FWHM, as shown in Fig. 2(c). The seed pulses are amplified up to 44 mJ before compression. A double-pass Treacy compressor with two multi-layer dielectric gratings (overall compression efficiency: 79%, resulting energy: 34.7 mJ) compresses the output pulses to 4.7 ps FWHM (assuming a Gaussian fit) as shown in the autocorrelation trace in Fig. 2(b), close to the transform limit pulse duration. The beam is magnified and collimated to 10 mm diameter ($1/e^2$) at the entrance of the compressor and remains collimated after the compressor.

The compressed output beam is sent to a TPF setup as shown in Fig. 2(a) to generate THz pulses. The input laser beam is diffracted to the minus one order by a gold-coated blazed grating with a groove density of 1500 lines/mm and a diffraction efficiency of 92% to obtain the desired tilted pulse front. The angle of incidence on the grating and the corresponding diffracted angle are 56.2° and 45.5° , respectively. The diffracted beam is imaged with a demagnification factor of -0.5 onto the exit surface of a cLN prism by two cylindrical lenses (tangential focal length: 75 mm, sagittal focal length: 50 mm). The pulse front tilt is then calculated to be 63.1° at the exit of the prism and can be tuned experimentally with the imaging system. A half-wave plate is used to rotate the polarization of the diffracted beam from p- to s-polarization, which is parallel to the extraordinary axis of the normal z-cut cLN prism.

The cLN crystal is a prism with a triangle base with $13.8 \times 13.8 \times 13.0 \text{ mm}^3$ dimensions, a height of 12.7 mm and an apex angle of 56° , corresponding to a phase-matching and pulse front tilt angle of 62° . The crystal is doped with 5.0 mol/% MgO to increase the damage threshold and reduce photorefractive effects [36]. The cLN prism is not anti-reflection (AR) coated for the IR, thus the IR pulses encounter 15% Fresnel losses. In the following, all the IR-input energies are given corrected for the losses of the imaging setup and for the Fresnel losses at the entrance of the crystal, *i.e.* are given inside the crystal, at its entrance. This corresponds to the useful energy for THz generation. Experimentally, we measured the energy at the entrance of the crystal to decrease from 34.7 mJ to 25 mJ due to various losses on optics on the way, thus the remaining IR input useful energy contributing for THz

generation is only 21 mJ. For all the measurements, the THz output facet of the prism is AR coated for the THz wave with a polyimide layer of 125 μm thickness; the estimated enhancement of the out-coupled THz energy compared to measurements taken without AR coating is 40%.

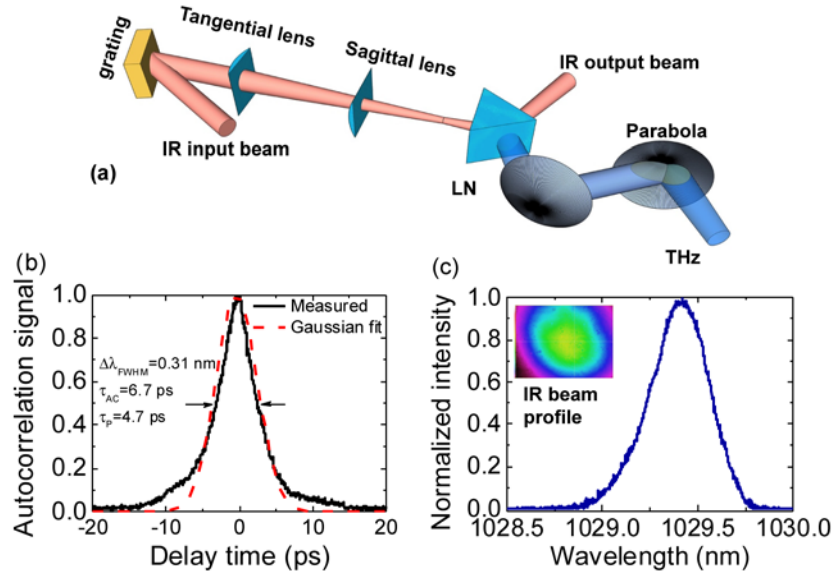


Fig. 2. Schematic of the experimental THz-TPF setup in (a) with the characteristics of the IR laser source: (b) shows the measured autocorrelation of the 1030nm IR input beam, fitted with a Gaussian function, and (c) its spectrum with the beam profile measured with a CCD in inset. LN stands for lithium niobate prism.

A custom-designed vacuum chamber is used together with a commercial dewar to cryogenically cool the cLN crystal down to 85 K with liquid nitrogen, reducing the absorption of the THz in the crystal and increasing the conversion efficiency. The temperature was monitored with a silicon temperature sensor mounted close to the crystal. The measurements at room temperature were taken with the vacuum chamber in place, to limit the changes in the setup, and make sure the focus point between sagittal lens and crystal was located in vacuum, avoiding possible nonlinear effects in air. The IR input and output fused silica windows on the chamber are broadband AR coated for 650-1030 nm and the THz window is a TPX (polymethylpentene) plate with 5-mm thickness, which has a flat transmission of 80% in the sub-THz range. In the following, the THz energy is given corrected by these calibration factors and called “extracted energy”.

The out-coupled THz pulses are collected in three different ways depending on the characterization to be done. In the case of energy measurements, the THz radiation is collected by two Teflon lenses (25 mm focal length, 90% transmission each) and measured by a pyroelectric detector (Gentec SDX-1152) covered with a silicon wafer to block the scattered light from the pump beam and the generated scattered green light in the cLN crystal. The conversion factor was $75 \mu\text{J/V}$, given by the manufacturer. A temperature sensitive liquid crystal sheet (Edmund Optics) was also used to visualize the intense focused THz beam directly after the vacuum chamber. For beam profile characterization, two 3-inch diameter off-axis parabolas (OAP) with 5-inch and 3-inch focal lengths each were used to image the THz beam onto a pyroelectric camera (Spiricon Pyrocam IV) covered by a 2-mm-thick silicon wafer. In order to characterize the temporal profile of the THz pulses, the THz beam is collected by two 2-inch diameter OAPs with 6-inch and 4-inch focal lengths respectively, and we performed an electro-optic sampling (EOS) measurement with a <110>-cut ZnTe crystal

with a thickness of 1.0 mm. A Glan-Taylor prism analysed the polarisation of the probe beam, and the signal was recorded with a photodiode.

3. Experimental results

3.1 Conversion efficiency and time-domain characterization

At room temperature, we first optimized the TPF setup at a pump energy of ~ 17.9 mJ in the crystal corresponding to a pump fluence of ~ 182.3 mJ/cm² and peak intensity of 38.8 GW/cm². We optimized the position of the crystal, the imaging system and also the chirp of the input pump pulses in the compressor. The optimization of the TPF setup is slightly different for different pump energies, because of the competition between THz generation and absorption inside the cLN crystal. The maximum efficiency of $\sim 0.08\%$ was obtained with the shortest pulse duration (4.7 ps); this corresponds to a maximum THz output energy of 14.6 μ J, as presented in Fig. 3(a). This energy conversion efficiency is close to the theoretical prediction of 0.095%, also plotted in Fig. 3(a). Note, that the THz efficiency curve keeps increasing with the pump fluence without showing obvious saturation, i.e. this measurement was limited by the available pump fluence. Figure 3(b) shows the IR spectra acquired before and after THz generation in the cLN crystal, with the vacuum chamber removed. Due to the cascading process, the IR output is spectrally broadened when the IR photons down convert to THz photons. In the OR process, as long as the phase matching condition is satisfied, THz photons are continuously generated inside the cLN crystal resulting in high optical-to-THz quantum efficiency. However, the angular dispersion in the cLN prism limits the amount of red-shifted IR photons reusable for cascaded THz generation, resulting in efficiency saturation. Our 2D theoretical model predicted a much larger red-shift at -10 dB than measured; the discrepancy might come from spatial averaging effects in the experiment: due to the Gaussian spatial intensity distribution of the driving IR beam, a higher conversion efficiency, i.e. a stronger shifts of the spectrum, is expected in the center of the beam than on the edges. The result of the 2D theory model would correspond to the spectrum acquired for the central part of the beam only. This is confirmed by our model including 3D spectral averaging; the simulation result shown in Fig. 2(b) agrees qualitatively with the measured data, even though the -10 dB level is located between 1022.5 nm and 1042.6 nm instead of 1028.8 nm and 1030.2 nm.

Congruent lithium-niobate has a strong linear absorption, measured to be 6.2 cm⁻¹ for 0.4 THz [30] and extrapolated from [29] for our simulations to 4.94 cm⁻¹ for 0.1 THz at room temperature, which prevents the THz radiation being out-coupled from the generation crystal. Cryogenic cooling of the crystal decreases the phonon vibrations and thus the absorption coefficient to 1.3 cm⁻¹ (for 0.4 THz at 50 K) [30]; in our simulations, we extrapolated an absorption coefficient of 0.52 cm⁻¹ at 85 K and 0.1 THz. Table 1 summarizes the parameters used in our simulations.

To further increase the THz output energy as well as the energy conversion efficiency, we raised the IR pump energy up to 21.3 mJ in the crystal while cryogenically cooling the crystal. Figure 3(c) shows the THz output energy and efficiency curves measured at the lowest achievable temperature of 85 K. Note that the TPF setup was optimized at cryogenic temperature for the 21.3 mJ pump energy. For different crystal temperatures, the optimal condition for efficient THz generation differs due to the modification of the refractive index, the tilt angle and effective interaction length with temperature. With a pump energy of 21.3 mJ, we obtained the maximum THz output energy of 65 μ J corresponding to a 0.3% conversion efficiency, as shown in Fig. 3(c). To the best of our knowledge, this is the highest THz pulse energy and efficiency measured at this low THz frequency. In this cryogenic cooling case, the efficiency curve shows the onset of saturation at a pump energy of ~ 15 mJ: increased cascaded down conversion from the IR to THz range increases the efficiency in comparison to the room temperature case. Due to the large divergence of the IR output beam

after the cLN crystal and geometrical constraints on the vacuum chamber, we could not measure the IR output spectrum at cryogenic temperature.

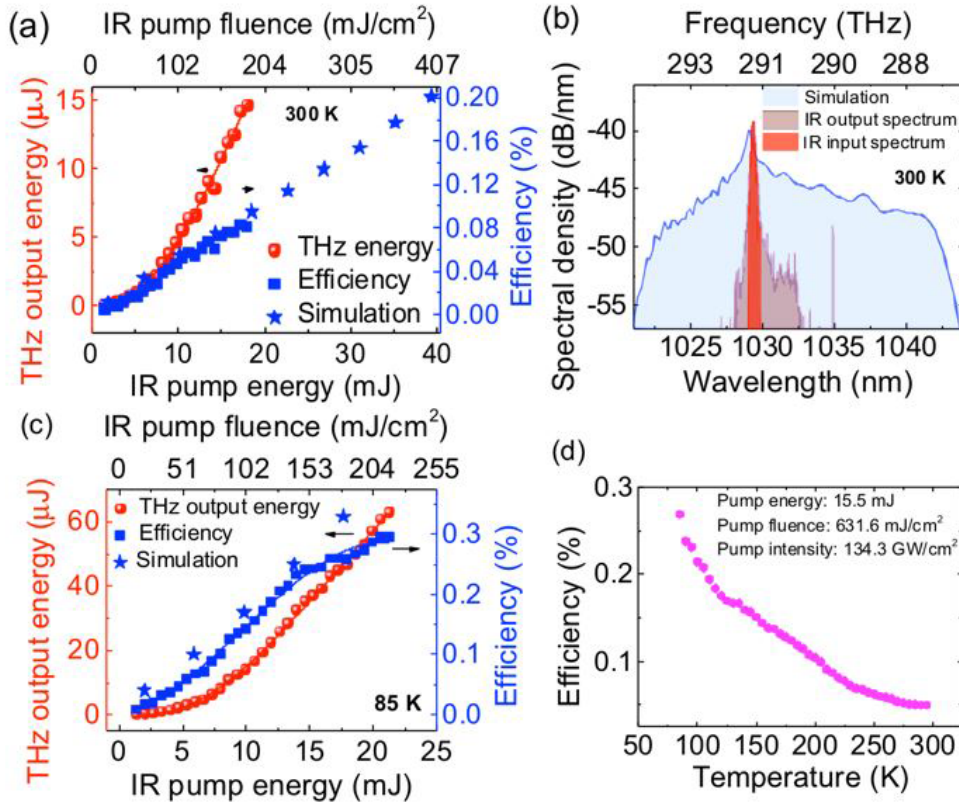


Fig. 3. Extracted and simulated output THz energy and efficiency at room temperature (300 K) (a) and cryogenic temperature (85 K) (c) versus IR pump energy and corresponding pump fluence calculated for a Gaussian beam. (b) Normalized measured IR-input and output spectra obtained at room temperature. The broadening towards longer wavelengths due to the cascading effect during THz generation is visible. The predicted IR-spectrum is also indicated. (d) Conversion efficiency versus temperature when the setup was optimized at 85 K.

Table 1. Simulation Parameters: Material and Numerical Parameters

d_{eff} pm/V	n_2 cm^2/W	α (300K) cm^{-1}	α (85K) cm^{-1}
168	$1\text{e-}15$	4.94	0.52
Longitudinal discretization	Transverse discretization	Bandwidth	Bandwidth discretization
μm	μm	THz	THz
1.25	50	110	0.05

Increasing the fluence on the crystal, above 0.3 J/cm^2 , the conversion efficiency is overall expected to be limited to 0.67%, according to our simulations. Experimentally, this has to be mitigated with the damage threshold of lithium niobate: the fluence has to be restricted to $0.2\text{--}0.4 \text{ J/cm}^2$, according to our own damage threshold measurements and to [37], to operate a factor 2 below damage threshold.

Figure 3(d) shows the measured optical-to-THz energy conversion efficiency as a function of crystal temperature. The curve was recorded following the steps below. We first optimized the whole setup at 85 K and for the available pump energy of 15.5 mJ and then waited for the

crystal to warm up to room temperature. We added liquid nitrogen and recorded the THz output energy for each temperature point. The energy conversion efficiency increases nonlinearly from 0.05% to 0.27% when the crystal temperature decreases from 295 K to 85 K. Note that the efficiency at 295 K is lower than the highest efficiency of 0.08% in Fig. 2(a) due to different optimization conditions for different pump energies and crystal temperature.

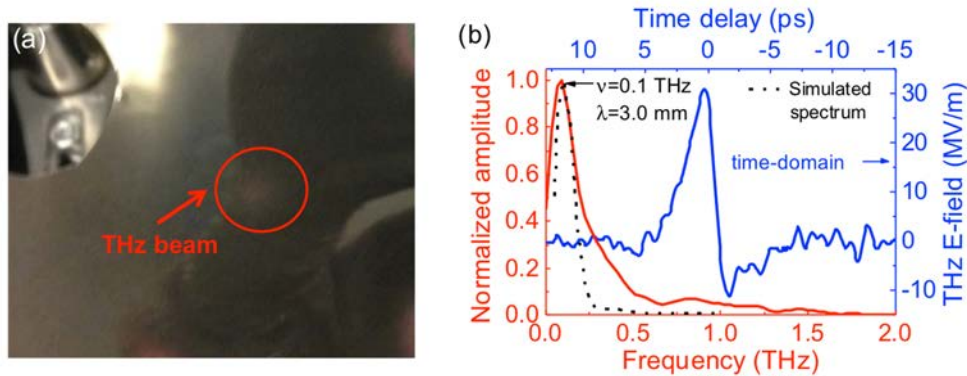


Fig. 4. Characteristics of the THz output for the highest energy achieved. (a) THz beam visualized on a liquid crystal sensor. (b) Electro-optic sampling of the THz pulse measured in the time-domain and calculated back in the frequency domain. The dot line shows the THz output spectrum obtained from numerical simulations.

For the first time the strong field THz pulses can be visualized by its polarizing effects on a liquid crystal plate, despite the low repetition rate of 100 Hz and consequently low average power, as can be seen in Fig. 4(a). To confirm that the central frequency of the generated THz wave is in agreement with the expected one, we measured the THz temporal waveform via EOS with the results shown in Fig. 4(b). This single-cycle THz pulse has a pulse duration of ~10 ps as predicted by theory. The peak frequency of the emitted THz pulse is exactly 0.1 THz corresponding to 3.0 mm wavelength. These results match very well with numerical simulations.

3.2 Spatial characterization

For any applications such as electron acceleration [11, 12], nonlinear THz field-matter interaction and spectroscopy [38] *etc.*, the beam profile and spatial properties of the intense THz beams are essential. As has been predicted in [34] and reported in [39], there exist nonlinear distortions of the spatial properties of the THz beam when generated via the TPF method. The generated THz beam size and its position in the horizontal direction will vary with variations of the pump energy. This is due to the variation of the effective interaction length inside the generation crystal for large pump beams and it has been observed for higher THz frequency generation with shorter pump laser pulses [39]. This analysis can be similarly done for the 0.1 THz radiation.

We measured the variation of the diameter and the displacement of the near-field THz beam at different pump energies by using a pyroelectric beam profiling camera after the imaging setup using the 3-inch OAPs in a confocal configuration, as shown in Fig. 5(a)-(c). Note that the output THz beam profile was optimized to be the smallest and the most circular at the highest IR pump energy at 85 K and then we decreased the pump energy to record the variation of the THz beam. Therefore, we obtained a circular beam profile for higher pump energy while the beam showed some ellipticity due to the slight movement of the generated beam inside the crystal and the imaging system not optimized at lower pump energies. The vertical error bars are calculated from the energy fluctuations of the laser (~2%), which translates into position and diameter fluctuations.

This measurement shows that, for different pump energies, the centroid position of the near-field THz beam does not change (Fig. 5(b)) but the beam diameter for both horizontal and vertical directions vary slightly by ~ 0.1 - 0.2 mm, corresponding to a 3-6% increase in beam diameter (Fig. 5(c)). This is much less than the reported variation of ~ 0.4 mm of the 2.1 mm diameter beam at high energy, i.e. 19%. There may be several possible reasons. Firstly, the lower conversion efficiency for the 0.1 THz radiation compared to the percent-level of the 0.3-0.5 THz generation [23–25] makes the nonlinear distortion less obvious. Secondly, the focused beam size achievable with the 0.1 THz pulses, i.e. with a longer wavelength of 3 mm, is larger than that from the >0.3 THz beam, resulting in less resolved nonlinear distortion. Thirdly, our characterization was performed at low temperature and the absorption coefficient inside the crystal is smaller for lower THz frequencies resulting in less variation of the effective interaction length for different pump energies. In consequence, the variation of the beam position and the beam size becomes less obvious at low temperature than room temperature. By choosing the OAPs to reach the highest possible demagnification, we focussed the THz beam down to ~ 2.5 mm diameter ($1/e^2$). Based on the measured THz output energy, pulse duration and beam size, we calculate the THz peak field strength to be 31.6 MV/m. This is the highest reported peak field strength generated at 100 GHz frequencies with an optical driver and enables the generation of 25 keV electrons directly from a metal surface, when transformed into a radially polarized beam, which will be explored elsewhere.

In order to further confirm that the THz beam has little nonlinear distortions, we also performed a far-field scan measurement in the horizontal direction, which has been reported to have more possibility to vary than the vertical one [35]. For this, an iris with variable aperture was placed before the THz detector to minimize spatial averaging effects and the transmitted THz energy was recorded versus the horizontal position of the detector and iris assembly. The distance between the cLN output facet and the THz detector was set to 123 mm, corresponding to a Fresnel number of 0.004, i.e. to a plane located in the far-field, and the result is shown in Fig. 5(d) for different IR input energies. After a Gaussian fit of the beam profile, the beam radius depending on intensity was found to vary between 10.9 and 11.6 mm at $1/e^2$. This slight change of the THz beam profile for different pump fluences is in agreement with the near-field imaging measurement. The last measurement shown in Fig. 5(e) is the direct measurement of the divergence of the THz beam. The beam radius is extrapolated from three measurements with the iris and detector assembly at different locations along the propagation from the THz facet of the cLN crystal. The half divergence angle is then calculated to be between 20.1° and 23.3° depending on the intensity. From the divergence formula of a Gaussian beam with an M^2 parameter of 1, this corresponds to a waist size of 2.4 ± 0.2 mm. According to simulations however, the THz beam size at the point of generation should be 5 mm.

The propagation through the imaging system can be calculated via ABCD matrices or via Fresnel propagation. The energy collected by the first OAP, with 3" aperture and 5" focal length, is about 70%. The available apertures of the OAPs are actually not sufficient to collect all the THz energy: less than one $1/e^2$ radius of the beam is collected. The imaging used for the energy measurement leads to 95% of energy collection. This means that our THz generation is actually slightly more efficient than what we are able to extract, collect and thus what would be usable for further experiments.

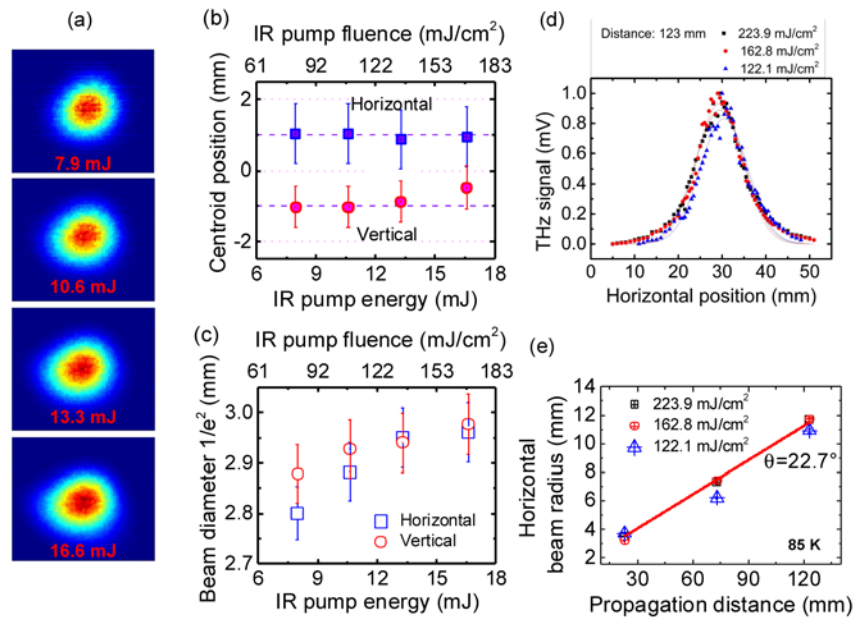


Fig. 5. Spatial characterization of the THz beam. (a)-(c) are measurements of the focused THz beam: (a) shows the beam profile acquired with a THz camera after collection and focusing with two OAP for different IR input energies. The location of the centroid of the beam is represented versus IR input pump energy and fluence in (b) and the evolution of the beam diameter in (c). The knife-edge measurement of the beam diameter in the far-field is shown in (d) and the measured THz beam divergence in the horizontal plane is shown in (e).

4. Conclusion

We have demonstrated in this work a high-energy, single-cycle strong-field 0.1 THz source via optical rectification in lithium-niobate driven by mJ-level, 4.7-ps, 1030-nm, 100-Hz laser pulses delivered by a cryogenically cooled Yb:YAG rod amplifier. We obtained a high optical-to-THz energy conversion efficiency of 0.3% at 85 K in agreement with the theoretical prediction resulting in a THz output energy of 65 μJ and a record peak field of 31.6 MV/m when focused to 2.5 mm diameter at $1/e^2$. An EOS measurement confirmed the central frequency of 0.1 THz; the electric field corresponds to a single-cycle pulse and the pulse duration is ~ 10 ps. The spatial characteristics of the THz radiation show less nonlinear distortion than the higher frequency THz sources. This in combination with the low divergence enables this 100 GHz single-cycle source to be stable and have performances well-suited for applications such as electron acceleration and nonlinear THz field-matter interaction and spectroscopy. We also expect that this table-top, optically-pumped intense 0.1 THz source will open the way to new applications such as sub-100 fs electron guns suitable for ultrafast electron diffraction and microscopy.

Funding

European Research Council under the European Union's Seventh Framework Programme (FP/2007-2013) / ERC Grant Agreement (609920); Deutsche Forschungsgemeinschaft; Alexander von Humboldt Foundation; Helmholtz Postdoctoral grant.